APPLIED PHYSICS

Twist angle–dependent valley polarization switching in heterostructures

Danjie Dai[1,2], Bowen Fu[3], Jingnan Yang[3], Longlong Yang[3], Sai Yan[1,2], Xiqing Chen[3], Hancong Li[3], Zhanchun Zuo[1,2], Can Wang[1,2,4]*, Kuijuan Jin[1,2,4], Qihuang Gong[3,5], Xiulai Xu[3,5]*

Copyright © 2024 The Authors, some rights reserved; exclusive licensee American Association for the Advancement of Science. No claim to original U.S. Government Works. Distributed under a Creative Commons Attribution NonCommercial License 4.0 (CC BY-NC).

The twist engineering of moiré superlattice in van der Waals heterostructures of transition metal dichalcogenides can manipulate valley physics of interlayer excitons (IXs), paving the way for next-generation valleytronic devices. However, the twist angle–dependent control of excitonic potential on valley polarization is not investigated so far in electrically controlled heterostructures and the physical mechanism underneath needs to be explored. Here, we demonstrate the dependence of both polarization switching and degree of valley polarization on the moiré period. We also find the mechanisms to reveal the modulation of twist angle on the exciton potential and the electron-hole exchange interaction, which elucidate the experimentally observed twist angle–dependent valley polarization of IXs. Furthermore, we realize the valley-addressable devices based on polarization switch. Our work demonstrates the manipulation of the valley polarization of IXs by tunning twist angle in electrically controlled heterostructures, which opens an avenue for electrically controlling the valley degrees of freedom in twistronic devices.

INTRODUCTION

Van der Waals (vdW) heterostructures, composed of two-dimensional transition metal dichalcogenides (TMDs), exhibit a type-II alignment. This alignment allows for the vertical stacking of two distinct monolayers (MLs) of TMDs, facilitating the generation of electrons and holes in separate layers (*1*–*4*). This spatial separation between electrons and holes results in a small overlap of their wave functions, leading to prolonged lifetimes of interlayer excitons (IXs) on the order of nanoseconds. The spatial separation of IXs carriers also gives rise to an out-of-plane electric dipole moment, enabling the manipulation of exciton energy through an external electric field (*5*–*8*). Furthermore, the properties of IXs with specific valley polarizations have attracted substantial attention benefiting from their controllable band alignment and wave function distribution, which can be flexibly tuned by an electrical control (*9*–*11*). For example, the electrical gating can modulate the preserved degree of circular polarization (DCP) of IXs by changing the valley depolarization (*10*). The moiré superlattice introduces a periodic potential where the optical selection rule is determined by the atomic registry. The different local interlayer distances between the two local potential minima allow their potential difference to be modulated by the electric field, therefore enabling the valley states of these quasi-particles to be electrically tuned (*12*, *13*).

In addition to electrical control, the twist angle also offers an effective tool to manipulate electronic properties of IXs (*14*). Twist engineering has also been used to control the valley degrees of freedom. The twist angle can control the potential landscapes for IXs and momentum alignment of valleys, leading to the engineering of the spin-valley properties in TMD heterostructures (*15*, *16*). Introducing twist engineering into electronic devices provides an additional degree of freedom by which to modulate the excitonic potential, thereby enhancing controllability over valley properties and enabling spintronic devices with more functions, such as electrically switchable spin-valley–based devices. However, the experimental demonstration of twist angle–dependent valley polarization in electrically controlled heterostructures is still missing. Meanwhile, deeper mechanisms underneath that how the moiré period govern the polarization switching by modulating the excitonic potential also remains to be further explored.

In this work, we demonstrate the dependence of both polarization switching and degree of valley polarization on the moiré period in electrically controlled heterobilayers (hBLs), enabling the precise control through twist engineering. We experimentally observe the twist angle–dependent valley polarization, clarified by the mechanism that considers the contributions of interlayer and intralayer to excitonic potentials and electron-hole (e-h) interactions. We also observe a complete polarization reversal to the twisted heterostructure. The critical gate voltage required for the valley state switching of IXs increases with the twist angle. We propose a theory by considering the excitonic potential difference on the moiré period, which reveals the mechanism underneath the twist angle–dependent polarization switching. Furthermore, we successfully demonstrate a valley-addressable encoding device based on valley polarization switching with IXs, where a periodic reversal of DCP and energy shift of IXs under a periodic bias voltage are obtained.

RESULTS

Optical characterizations of WSe_2/WS_2 hBLs

ML WSe_2 and ML WS_2 were first obtained by chemical vapor deposition (CVD) and then were sequentially transferred onto silica substrates by a wet transfer method to form WSe_2/WS_2 twisted hBLs. The twist angles were roughly estimated with an optical microscope (fig. S1) and then further confirmed by using the second harmonic generation spectroscopy (fig. S2). The weak vdW force in heterostructures allows a stacking of lattice mismatch between the constituent layers (*4*). The twist between two layers in real space leads to the emergence of moiré periodic patterns, as shown in Fig. 1A. In this periodic pattern, three high-symmetry points (inset of Fig. 1A)

[1]Beijing National Laboratory for Condensed Matter Physics, Institute of Physics, Chinese Academy of Sciences, Beijing 100190, China. [2]CAS Center for Excellence in Topological Quantum Computation and School of Physical Sciences, University of Chinese Academy of Sciences, Beijing 100049, China. [3]State Key Laboratory for Mesoscopic Physics and Frontiers Science Center for Nano-optoelectronics, School of Physics, Peking University, Beijing 100871, China. [4]Songshan Lake Materials Laboratory, Dongguan, Guangdong 523808, China. [5]Peking University Yangtze Delta Institute of Optoelectronics, Nantong, Jiangsu 226010, China.
*Corresponding author. Email: xlxu@pku.edu.cn (X.X.); canwang@iphy.ac.cn (C.W.)

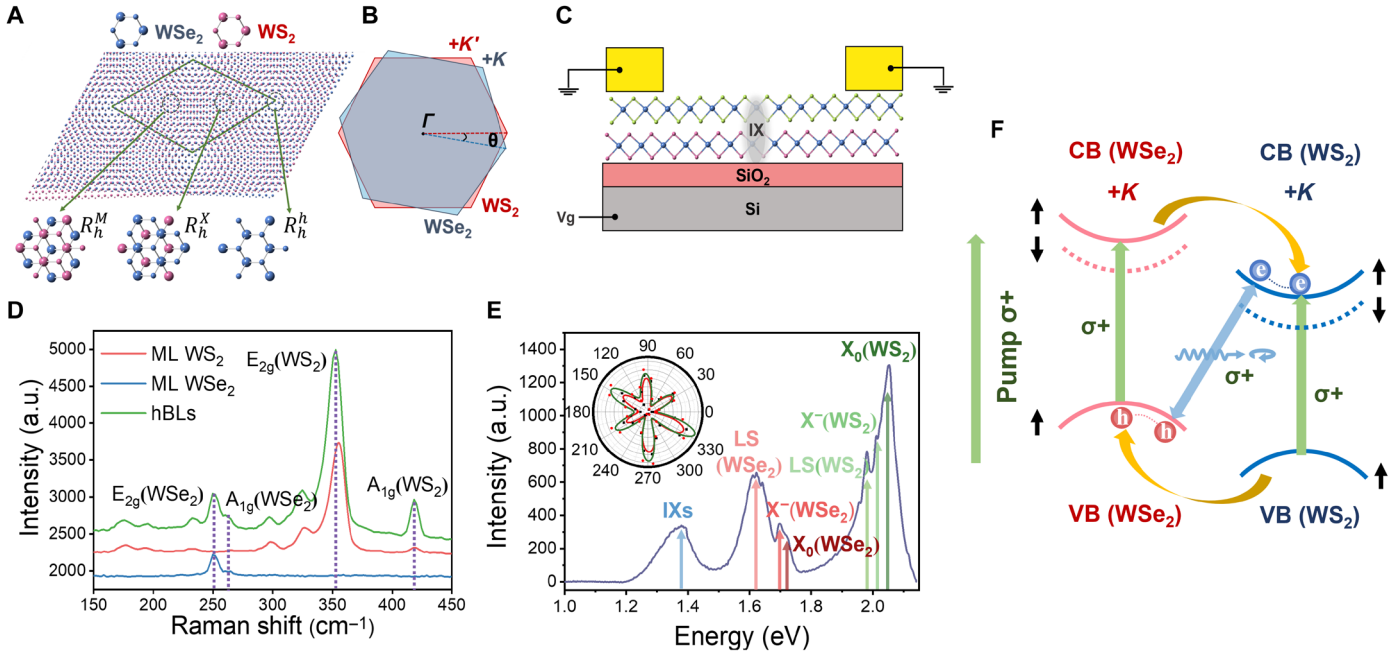

Fig. 1. Device characterization. (**A**) Moiré pattern formed by stacking two MLs. The area marked by the green diamond represents one moiré period, which includes three extreme points. The inset shows a zoom-in of these three locations. (**B**) Schematic of the Brillouin zone of ML WS_2 (red) and ML WSe_2 (blue) with a twist angle of θ. (**C**) Schematic of the device structure. (**D**) Raman spectra of ML WSe_2 (blue line), ML WS_2 (red line), and hBLs (green line) at room temperature. (**E**) Low-temperature ($T = 10$ K) PL spectrum of $\theta \approx 0°$ device. Inset: Second harmonic generation measurement of the heterojunction with $\theta \approx 0°$. (**F**) Schematic illustration of the formation of IXs in $+K$ valley with 3R stacking. The black arrows denote the spin orientation of the conduction and valence bands, respectively. The green lines indicate σ+ excitation in both WS_2 and WSe_2 layers. The yellow arrows delineate the charge transfer process. The blue arrows symbolize interlayer emission, where IXs inherit intralayer copolarized emission in the 3R-stacking configuration. a.u., arbitrary units.

with different local atomic registry inherit $\hat{C}_3$ symmetry (*12*, *17*, *18*). The unique interlayer optical selection rule is governed by the $\hat{C}_3$ rotation, where the interlayer transition at K ($-K$) point can couple with σ+ or σ− photons. Hence, exciton wave packets at these three locals have different $\hat{C}_3$ transformations, giving the different optical selection rules (*12*). Here, we use R_h^μ denoting the 3R stacking. Taking the hole-layer hexagon center (h) site as the rotation center, these three positions correspond to the electron-layer at h (R_h^h, site A), chalcogen (R_h^X, site B), and metal (R_h^M, site C). The twist in real space leads to a displacement in momentum space (Fig. 1B). This momentum mismatch can be compensated by the finite kinetic energy of the exciton (*4*, *19*). The valley shifts in each layer change the transformation at the $\pm K$ valleys from direct to indirect. The type-II energy bands are aligned so that the electrons and holes in the heterostructure are located at the energy minima in different layers (*6*, *11*).

As shown in Fig. 1C with our device configuration, optical characterization can be performed with electrical control. To confirm the interlayer coupling, both Raman and photoluminescence (PL) characterizations of the devices are investigated on the heterostructure. The Raman spectra of the heterostructure exhibit superimposed E_{2g} and A_{1g} modes of the two MLs (Fig. 1D). Figure 1E shows the PL of the heterostructure at low temperature ($T = 10$ K), where we observe the emission of ML WS_2 and ML WSe_2 as well as the interlayer emission. The green region shows the energy peaks of neutral exciton (X_0, 2.05 eV), charged exciton (X^-, 2.01 eV), and localized excitons (1.98 eV) for ML WS_2. The red region shows the energy peaks of neutral exciton (1.72 eV), charged exciton (1.70 eV), and localized state (LS; 1.62 eV) for ML WSe_2 (*20*–*22*), respectively. We attribute the emission with energy peak of 1.39 eV (IXs, blue) to the interlayer transition resulting from charge transfer. In comparison to the emission of pristine ML excitons at room temperature, the emission of intralayer excitons in heterostructure exhibits a red shift (fig. S3). The observed red shift can be attributed to the changes in the dielectric environment and charge transfer processes (*23*, *24*). The power dependence PL spectra of IXs are shown in section S3. As the power increases, the IXs undergo a blue shift in contrast to the red shift observed in intralayer emission, which is attributed to the repulsive dipole-dipole interactions (*5*, *7*, *25*).

Electrical tuning of valley polarization of IXs

The stacking of the ML WSe_2 and ML WS_2 forms a vdW heterostructures with type-II band alignment (Fig. 1F). Figure 2 (A and B) shows the gate-dependent PL spectra of the device with $\theta \approx 0°$. The energy of the IXs is modulated by gate voltage from Fig. 2C. The emission of IXs undergoes a blue shift with increasing gate voltage. An energy shift of about 80 meV is obtained when the gate voltage changed from −40 to 40 V. The shift of the IXs with the gate voltage is also controlled by the stacking configuration. With a reversed stacking order of the two MLs, an opposite shift in IXs is observed (fig. S5). Furthermore, selectively addressing the valley degree of freedom of excitons using circularly polarized light under a gate voltage is an important approach to understanding electrically tunable valley-contrasting physics of IXs (*6*, *10*). The DCP of IXs as a function of the gate voltage is shown in Fig. 2D, with PL intensities extracted from the emission intensities of σ+ and σ− (Fig. 2, A and

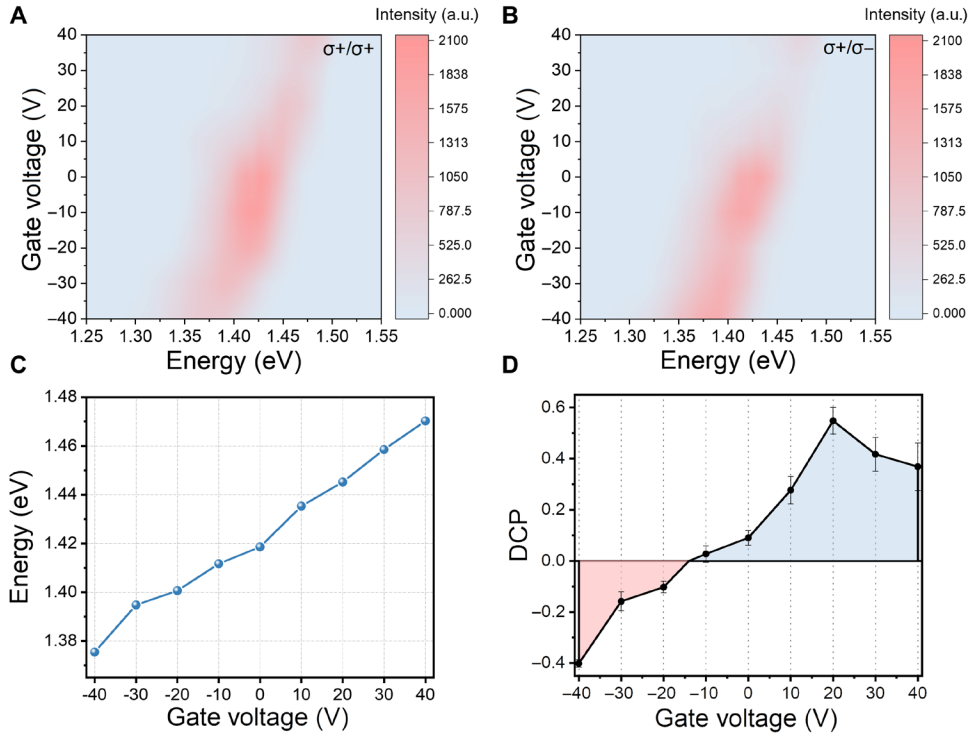

Fig. 2. Electrical control of the IXs in the device with θ ≈ 0°. (**A** and **B**) Contour plots of gate-dependent PL spectra ($T = 10$ K) using σ+ excitation with σ+ and σ− detection. (**C**) Energy shift of IXs as a function of the gate voltage. (**D**) DCP of PL spectra from IXs as a function of the gate voltage.

B). Here, the DCP is defined by $p = (I_+ - I_-)/(I_+ + I_-)$, where $I_{+(-)}$ represents the intensities of the σ+ and σ− circularly polarized emission with σ+ excitation. As illustrated in Fig. 2D, a predominant co-circular polarization of IXs is observed with a positive applied voltage, whereas a reversal of polarization is observed when applying a negative voltage of −20 V. Thus, this polarization switching can be attributed to the modulation of periodic excitonic potential by electrical controlling (*12*), where a spatial modulation of the electronic structure induces a shift of local minimum. These distinct local minima can be identified within moiré superlattices (Fig. 1A), with different $\hat{C}_3$ rotations and distinct optical selection rules (*17*, *26*).

Twist angle–dependent valley polarization of IXs

To clarify the dependence of valley polarization of IXs on the gating and moiré superlattice, Fig. 3 (A to C) shows the gate-dependent circular polarization of the IXs for the devices with three different twist angles (the full dataset is provided in fig. S6). For emissions of IXs, the reversal of polarization under negative bias is observed for all the devices with θ ≈ 0°, 1°, and 3°. The critical voltage required to enable the reversal of the circular polarization of the IXs becomes larger as the twist angle increases. For devices with θ ≈ 0°, θ ≈ 1°, and θ ≈ 3°, the reversal of the circular polarization of IXs occurs at biases close to −10, −20, and −30 V, respectively. We used density functional theory (DFT) theoretical calculations to determine the exciton potential of IXs at different twist angles. The calculation method is presented in section S9. IXs experience a periodic potential in a moiré superlattice, leading to variations in the excitonic potential difference between sites A and B for different moiré periods. The dependence of $\boldsymbol{r_0}$ (the displacement of the metal site in the hole layer to the nearest neighboring metal site in the electron layer) on twist angle in the moiré superlattice generally results in spatial modulation in the local bandgap of excitons, thereby affecting their excitonic potential (*12*). Figure 3 (E and F) shows the contour plots of excitonic potential in moiré patterns and diagonal scanning curves under zero gate voltage, respectively. When we set the twist angle to 1°, 2°, and 3°, the difference between V(A) and V(B) is calculated to be 94, 124, and 147 meV, respectively. As reported in the literature, the electrical effects to switch the polarization are diverse, including Stark shift (*12*), charge doping (*6*), or altering Hubbard (U) interaction (*27*, *28*), and specific details are still under discussion. Nonetheless, the theoretical result that V(A)-V(B) increases with the twist angle is general and indicates that a higher external potential is required for a device with larger twist angle to switch the PL polarization. This corresponds well with our experimental observations.

The interaction between the two constituent layers determines the strength of the interlayer coupling (*4*, *29*, *30*). When the twist angle between the two layers is away from 0° or 60°, the interlayer coupling gradually decreases to disappear because of a very low wave function overlap (*31*–*33*). When the twist angle exceeds 3.5°, the mismatch between the two layers cannot be ignored, and the interlayer coupling is expected to be weakened (*19*, *30*, *32*). The polarization-resolved PL spectra of devices with larger twist angles are also investigated for comparison as shown in fig. S7. A significant quenching of interlayer emission near 1.36 eV is observed, which is insensitive to gate voltage. No polarization difference can be resolved within the range of bias voltage applied. By using DFT calculation, the statistic distributions of interlayer distance also confirm that the interlayer spacing increases with the angle, leading to a weaker interlayer coupling (fig. S8), consistent with our experimental results.

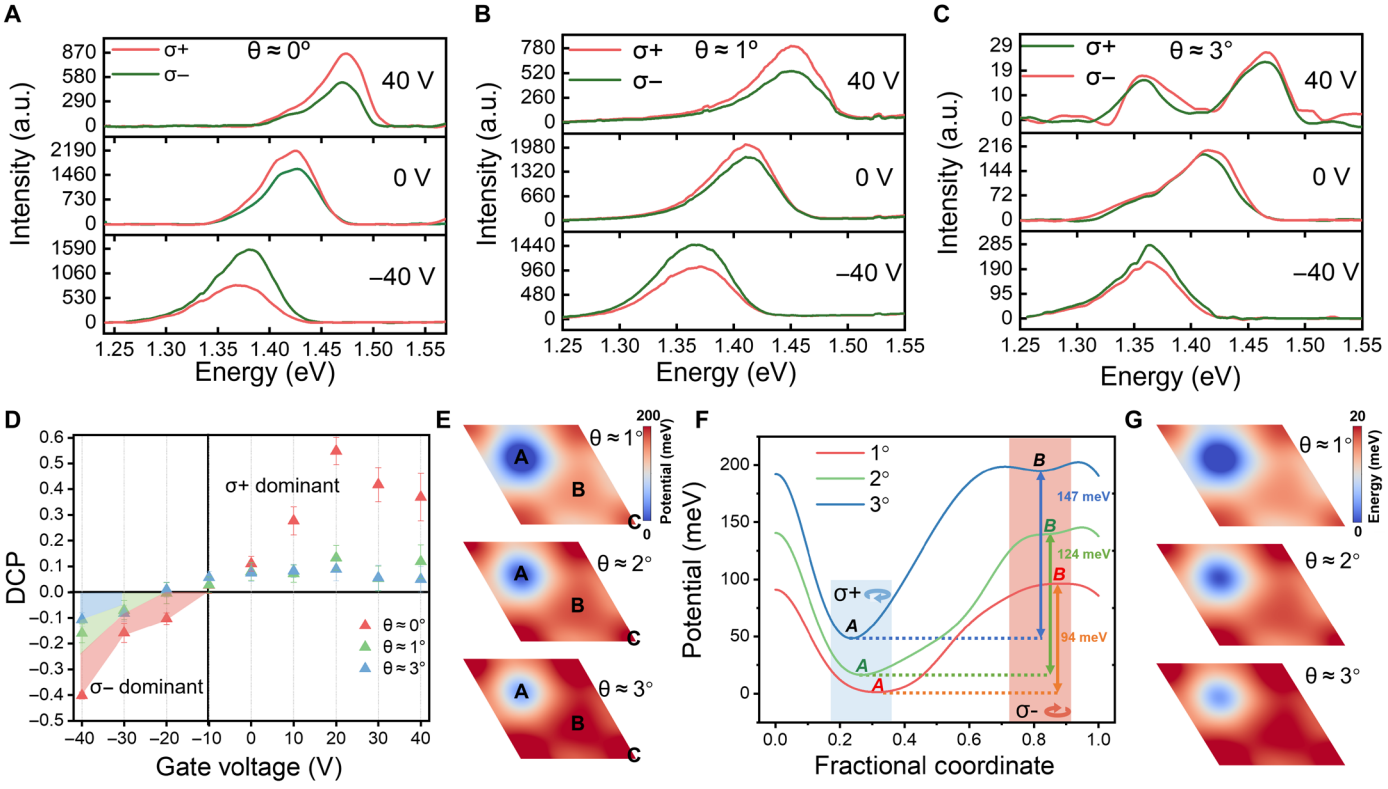

Fig. 3. Twist angle–dependent polarization properties. (**A** to **C**) Polarization-resolved PL spectra ($T = 10$ K) at −40, 0, and 40 V of $\theta \approx 0°$, $\theta \approx 1°$, and $\theta \approx 3°$. (**D**) DCP of IXs as a function of gate voltage of the three devices. (**E**) Contour plots of excitonic potential at varying twist angles. (**F**) Diagonal scanning curves from the contour plots at varying twist angles and interlayer optical selection rule of moiré excitons. (**G**) Contour plots of strength of interlayer e-h exchange energy.

Figure 3D depicts the DCP of IXs with different twist angles, indicating a reduction in the DCP of IXs as the twist angle increases. To further clarify the physical mechanism of the valley polarization variation induced by the moiré period, we investigate the interlayer and intralayer influences on the circular polarization of IXs. For the interlayer, the interlayer excitonic potential and the e-h exchange are dependent on the interlayer translation (*17*). It can be seen that the excitonic potential profile of site A increases with the increasing twist angle from Fig. 3 (E and F). Under zero gate voltage, site A denotes the global minimum in terms of energy, and the polarization selection rule at this point is determined by the moiré superlattice, with a σ+ polarization. A lower exciton potential at local minimum (site A) caused by larger moiré period results in a larger population of excitons trapped at A and thereby enhancing the emission of σ+. Similarly, when the electrical control switches the local minimum to site B, a smaller twist angle also results in an enhancement in the emission of σ−. To confirm the effect of moiré period on the interlayer e-h exchange interaction, the strength of the interlayer e-h exchange energy for different twist angles are also calculated. Figure 3G shows the contour plots of interlayer e-h exchange energy calculated with DFT, indicating that the strength of exchange interaction increases with twist angle. Exchange interactions between electrons and holes can intensify spin hybridization, thereby reducing the DCP of IXs. Therefore, the dependence of the interlayer e-h exchange energy and excitonic potential on the moiré periodicity induces a twist angle–dependent circular polarization of IXs.

In TMD heterostructures, IXs inherit the coupled spin-valley physics from constituent MLs, which enhances the interactions of internal degrees of freedom, including the spin and valley pseudospin of electrons and holes confined in different MLs (*17*, *24*, *34*). The interlayer transition dipoles are also controlled by the coupling with the intralayer valley excitons through interlayer hopping (*35*). Consequently, the observed interlayer valley polarization could depend on the depolarization of intralayer excitons before relaxation to interlayer state (*32*, *35*). Figure 1F illustrates the configuration of IXs in 3R stacking, with the electron and hole of the IXs located at the $+K$ valleys of WS_2 and WSe_2, respectively. Spin-polarized excitation allows the intralayer exciton to have an initial valley polarization. Then, an ultrafast interlayer charge transfer via spin conservation takes place before valley scattering, typically within a picosecond timescale (*2*, *23*, *36*). After that, the interlayer e-h pair radiatively recombines and emits photons that inherit the intralayer valley polarization.

E-h exchange interactions can cause valley scattering and reduce the DCP (*37*–*40*). Therefore, we investigate the intralayer exciton valley dynamics and e-h exchange energy at various twist angles to explore how initial intralayer valley polarization influences interlayer circular polarization through twist angles. Figure 4A depicts the time-resolved spectra of intralayer excitons (WS_2) in twisted heterostructures and pristine ML, with both copolarized and cross-polarized components. The green (red) dots represent σ− (σ+) detection. Figure 4B shows the time-resolved DCP with different twist angles. The solid line represents the data fitted with an exponential

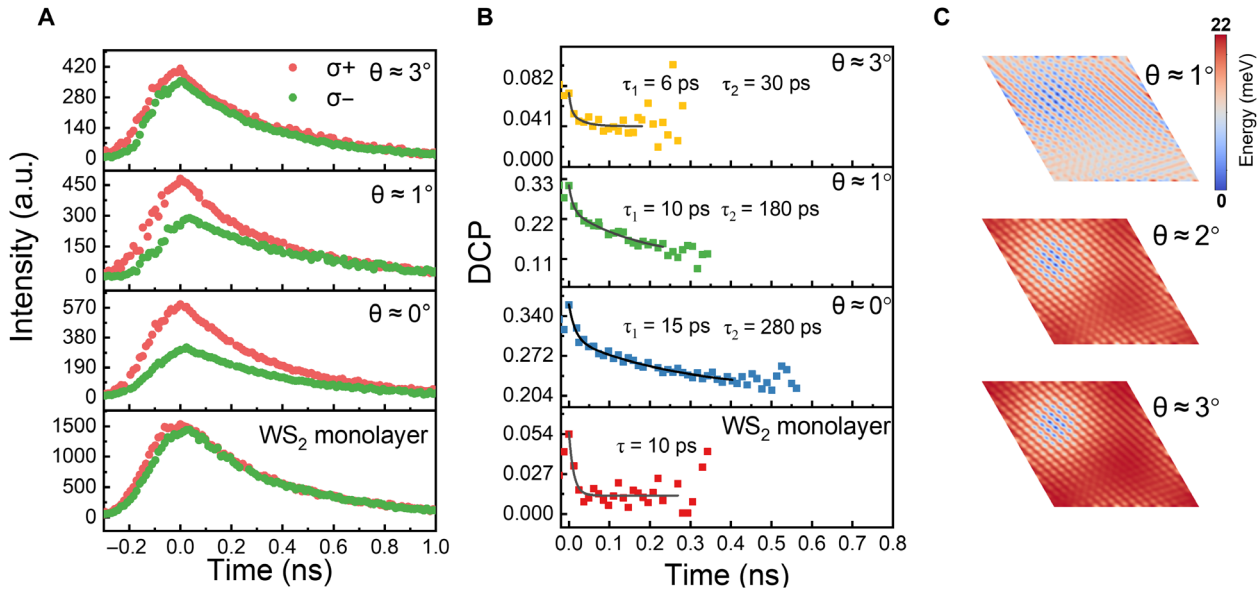

Fig. 4. Intralayer exciton valley dynamics in twisted hBLs. (**A**) Time-resolved measurements ($T = 10$ K) of co- and cross-polarized PL at varying twist angles. Green (red) dots represent cross (co)–polarized PL decay. (**B**) Time-resolved DCP corresponding to measurements in (A). Solid black lines represent the exponential fits of valley time. (**C**) Intralayer e-h exchange energy in WS_2 layer at different twist angles.

decay model. The valley lifetimes of intralayer excitons in the twisted heterostructures significantly decrease with increasing twist angle, accompanied by a gradual reduction in the DCP of IXs (Fig. 3). This shows that the moiré period can modulate the intralayer initial valley polarization and thus affect the DCP of the IXs (*32*). To explore the physical mechanism of initial valley lifetimes dependence on twist angle, we calculate the intralayer e-h exchange interactions for different moiré period. Figure 4C illustrates a significant increase in the strength of intralayer e-h exchange interactions with increasing twist angle, resulting in a decrease on the valley lifetime. It can be concluded that larger moiré period leads to an increase in the initial degree of valley polarization of intralayer photo-created carriers resulting in an enhancement in the valley polarization of IXs with decreasing twist angle. The spin-polarized density of states in twist heterostructures depicts that as the twist angle increases (fig. S9), the spin-polarized density at site A decreases, demonstrating a weakening chirality throughout the entire system, which is consistent with our results. Therefore, twist engineering in heterostructures can be used as a versatile tool to manipulate polarization of IXs.

Furthermore, the temperature-dependent valley polarization properties of IXs are also investigated for two devices with twist angles of 0° and 3° (section S7). The suppression of polarization with increasing temperature results from enhanced intervalley scattering and spin relaxation due to the phonon-mediated scatterings (*37*, *41*, *42*). For example, with a gate voltage of −40 V, the valley polarization of IXs reverses from σ− to σ+ with increasing temperature. This is why we focus on the low-temperature measurement to suppress the phonon scatterings in this work.

Valley-addressable switching

The information in valley-addressable devices can be stored, retrieved, and manipulated through the controlled excitation and detection of the valleys, enabling reading/erasing/writing operations on the memory units (*43*). To investigate the valley optical addressable of twist heterostructures, Fig. 5 shows time-dependent PL energy and DCP under periodic gate voltage modulation for devices with $\theta \approx 0°$ and $\theta \approx 1°$ under $T = 10$ K. Here, we detect the helicity switching between σ+ and σ− under the same gate voltage with σ+ excitation. For the device with $\theta \approx 0°$, when the gate voltage periodically varies into −40, 0, 40, and 0 V, the energy of the IXs also undergoes periodic changes into 1.38, 1.42, 1.47, and 1.42 eV. This energy modulation resembles the selective operations of encoding devices, such as writing, erasing, and reading, and exhibits repeatability during the periodic modulations. The sign of valley polarization undergoes periodic changes with the gate voltage as well. As shown in Fig. 5A (bottom), for the device with $\theta \approx 0°$, the sign of interlayer polarization changes from positive to zero and to negative with the periodic variation of gate voltages. Similar phenomena are obtained for the $\theta \approx 1°$ device with the periodic gate voltage at −40, −20, and 40 V, demonstrating the stability and reproducibility of our devices. Consequently, the spin state of the emitted photon can be encoded as 0 and 1 with different polarizations, respectively. They can represent different information bits being optically recognized and decoded. Compared to electronic memories, photon polarization–based memory may offer better integration with quantum photonics devices, thereby enabling more efficient storage and processing of quantum information, which can also be controlled optically. Our devices demonstrate the functions of reading/erasing/writing operations by selectively encoding the valley polarization information through different helicity excitation or detection.

DISCUSSION

We have demonstrated a manipulation of the polarization of the IXs by changing moiré period in the WSe_2/WS_2 hBLs with an electrical control. We observe that the devices with larger twist angles require a higher gate voltage to achieve polarization reversal, which can be

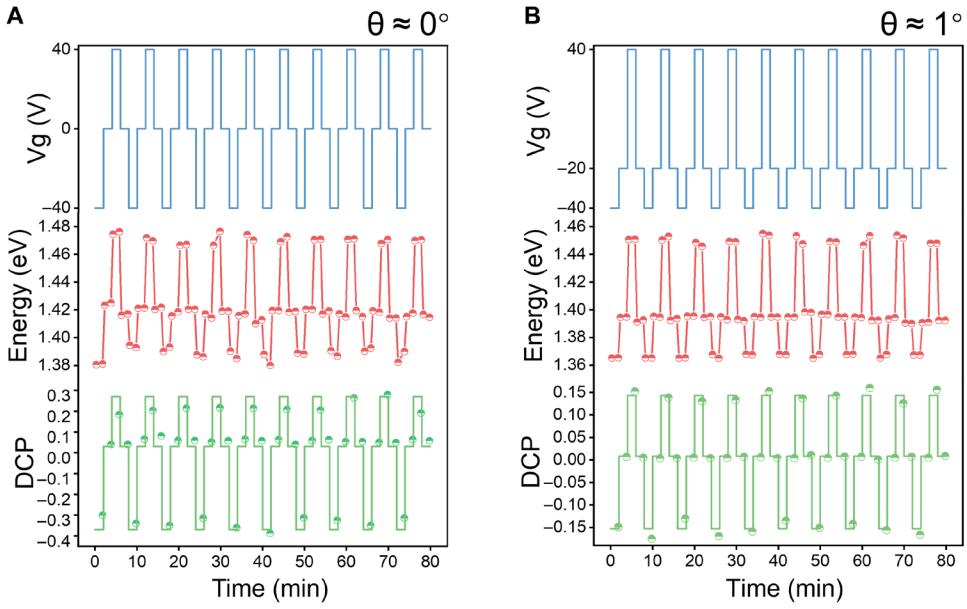

Fig. 5. Valley optical addressing in electrically controlled twist heterostructures. (**A** and **B**) Time-dependent energy (red dots) and DCP (green dots) of IX emission of devices (A) θ ≈ 0° and (B) θ ≈ 1° with a periodical bias voltage (blue lines). Each voltage lasts for 2 min with detecting σ+ or σ− polarizations.

clarified by our proposed theory based on the dependence of excitonic potential difference between local minima with different circularly polarized emissions on moiré period. Theoretical calculations confirm that the excitonic potential difference V(A)-V(B) increases with the twist angle, leading to a larger external potential for switching between A and B. The moiré signature governing the DCP of IXs is revealed with encompassing both interlayer and intralayer effects. The observed twist angle–dependent interlayer DCP can be explained well by the measurements of valley dynamics and our theoretical calculations of excitonic potential and e-h exchange interactions. A larger moiré period results in a reduction in the IX potential at the local minimum, a decrease in both interlayer and intralayer e-h exchange interactions, and an increase in the initial intralayer valley polarization, ultimately leading to an enhancement of degree of interlayer valley polarization. The experimental modulation of DCP and IX emission energy under periodic gate voltage indicates the potential for further implementation of nonvolatile memories through the construction of floating gates or substrate engineering. Photon polarization–based memory provides a favorable platform for integrating valley-addressable memory into quantum optical devices. This work unveils the physical mechanism for modulating interlayer circular polarization in twistronic systems and demonstrate the feasibility of precisely controlling polarization by manipulating the moiré period in electrically modulated hBLs.

MATERIALS AND METHODS

Device fabrication

WSe_2 and WS_2 MLs were grown by a CVD system, which were subsequently transferred onto Si/SiO_2 substrates using a wet transfer method, resulting in WSe_2/WS_2 hBLs with different twist angles. To obtain clean interfaces and enhance the interlayer coupling, each transfer step was followed by an ultrahigh vacuum annealing process at 160°C for 1 hour. The Au electrodes on the upper layer of the two-dimensional materials were fabricated with the electron beam lithography and the thermal evaporation (5-nm Cr/50-nm Au). A final annealing process was conducted after the electrode fabrication to effectively eliminate organic residues from the material surface.

Optical measurements

The devices were mounted on a three-dimensional piezoelectric stage in a temperature-controlled chamber ranging from 4.4 to 300 K. PL and Raman measurements were conducted using 532-nm continuous wave laser excitation. Except for room temperature Raman spectroscopy, all characterizations were performed at 10 K using a confocal microscope system with a 0.82–numerical aperture objective. The signal was collected through a grating spectrometer and recorded by a liquid nitrogen–cooled charge-coupled device (CCD) detector. The signal was acquired through a grating spectrometer with a liquid nitrogen–cooled CCD detector. For all polarization-resolved PL, the circularly polarized excitation was selectively excited by using a linear polarizer and a quarter–wave plate, and the PL circularly polarized emissions are collected by using a quarter–wave plate and a linear polarizer in front of the spectrometer. For second harmonic generation measurement, the laser pulse with a central wavelength of 800 nm from a Ti:sapphire laser was used and focused on the sample with a microscope objective. The second harmonic signal was collected by the same objective and detected with a spectrometer. Time-resolved spectroscopy was performed with a time-correlated single-photon counting method. A pulsed laser with a wavelength of 532 nm was used to pump the sample, and the spin-polarized PL was collected by a single-photon detector.

Supplementary Materials

This PDF file includes:

Sections S1 to S9
Figs. S1 to S12
References

REFERENCES AND NOTES

1. Q. Tan, A. Rasmita, S. Li, S. Liu, Z. Huang, Q. Xiong, S. A. Yang, K. S. Novoselov, W.-B. Gao, Layer-engineered interlayer excitons. *Sci. Adv.* **7**, eabh0863 (2021).
2. C. Jin, E. Y. Ma, O. Karni, E. C. Regan, F. Wang, T. F. Heinz, Ultrafast dynamics in van der Waals heterostructures. *Nat. Nanotechnol.* **13**, 994–1003 (2018).
3. Y. Hu, X. Wen, J. Lin, W. Yao, Y. Chen, J. Li, S. Chen, L. Wang, W. Xu, D. Li, All-optical valley polarization switch via controlling spin-triplet and spin-singlet interlayer exciton emission in WS_2/WSe_2 heterostructure. *Nano Lett.* **23**, 6581–6587 (2023).
4. P. Rivera, H. Yu, K. L. Seyler, N. P. Wilson, W. Yao, X. Xu, Interlayer valley excitons in heterobilayers of transition metal dichalcogenides. *Nat. Nanotechnol.* **13**, 1004–1015 (2018).
5. L. A. Jauregui, A. Y. Joe, K. Pistunova, D. S. Wild, A. A. High, Y. Zhou, G. Scuri, K. De Greve, A. Sushko, C. H. Yu, T. Taniguchi, K. Watanabe, D. J. Needleman, M. D. Lukin, H. Park, P. Kim, Electrical control of interlayer exciton dynamics in atomically thin heterostructures. *Science* **366**, 870–875 (2019).
6. A. Ciarrocchi, D. Unuchek, A. Avsar, K. Watanabe, T. Taniguchi, A. Kis, Polarization switching and electrical control of interlayer excitons in two-dimensional van der Waals heterostructures. *Nat. Photonics* **13**, 131–136 (2019).
7. M. Brotons-Gisbert, H. Baek, A. Campbell, K. Watanabe, T. Taniguchi, B. D. Gerardot, Moiré-trapped interlayer trions in a charge-tunable $WSe_2/MoSe_2$ heterobilayer. *Phys. Rev. X* **11**, 031033 (2021).
8. H. Baek, M. Brotons-Gisbert, Z. X. Koong, A. Campbell, M. Rambach, K. Watanabe, T. Taniguchi, B. D. Gerardot, Highly energy-tunable quantum light from moiré-trapped excitons. *Sci. Adv.* **6**, eaba8526 (2020).
9. C. Jiang, W. Xu, A. Rasmita, Z. Huang, K. Li, Q. Xiong, W. B. Gao, Microsecond dark-exciton valley polarization memory in two-dimensional heterostructures. *Nat. Commun.* **9**, 753 (2018).
10. P. Rivera, K. L. Seyler, H. Yu, J. R. Schaibley, J. Yan, D. G. Mandrus, W. Yao, X. Xu, Valley-polarized exciton dynamics in a 2D semiconductor heterostructure. *Science* **351**, 688–691 (2016).
11. G. Scuri, T. I. Andersen, Y. Zhou, D. S. Wild, J. Sung, R. J. Gelly, D. Berube, H. Heo, L. Shao, A. Y. Joe, A. M. Mier Valdivia, T. Taniguchi, K. Watanabe, M. Loncar, P. Kim, M. D. Lukin, H. Park, Electrically tunable valley dynamics in twisted WSe_2/WSe_2 bilayers. *Phys. Rev. Lett.* **124**, 217403 (2020).
12. H. Yu, G. B. Liu, J. Tang, X. Xu, W. Yao, Moiré excitons: From programmable quantum emitter arrays to spin-orbit-coupled artificial lattices. *Sci. Adv.* **3**, e1701696 (2017).
13. H. Yu, G.-B. Liu, W. Yao, Brightened spin-triplet interlayer excitons and optical selection rules in van der Waals heterobilayers. *2D Mater.* **5**, 035021 (2018).
14. K. Wu, H. Zhong, Q. Guo, J. Tang, J. Zhang, L. Qian, Z. Shi, C. Zhang, S. Yuan, S. Zhang, H. Xu, Identification of twist-angle-dependent excitons in WS_2/WSe_2 heterobilayers. *Natl. Sci. Rev.* **9**, nwab135 (2022).
15. J. Quan, L. Linhart, M. L. Lin, D. Lee, J. Zhu, C. Y. Wang, W. T. Hsu, J. Choi, J. Embley, C. Young, T. Taniguchi, K. Watanabe, C. K. Shih, K. Lai, A. H. MacDonald, P. H. Tan, F. Libisch, X. Li, Phonon renormalization in reconstructed MoS_2 moiré superlattices. *Nat. Mater.* **20**, 1100–1105 (2021).
16. Y. Cao, V. Fatemi, A. Demir, S. Fang, S. L. Tomarken, J. Y. Luo, J. D. Sanchez-Yamagishi, K. Watanabe, T. Taniguchi, E. Kaxiras, R. C. Ashoori, P. Jarillo-Herrero, Correlated insulator behaviour at half-filling in magic-angle graphene superlattices. *Nature* **556**, 80–84 (2018).
17. H. Yu, Y. Wang, Q. Tong, X. Xu, W. Yao, Anomalous light cones and valley optical selection rules of interlayer excitons in twisted heterobilayers. *Phys. Rev. Lett.* **115**, 187002 (2015).
18. Y. Wang, Z. Wang, W. Yao, G.-B. Liu, H. Yu, Interlayer coupling in commensurate and incommensurate bilayer structures of transition-metal dichalcogenides. *Phys. Rev. B* **95**, 115429 (2017).
19. J. Choi, M. Florian, A. Steinhoff, D. Erben, K. Tran, D. S. Kim, L. Sun, J. Quan, R. Claassen, S. Majumder, J. A. Hollingsworth, T. Taniguchi, K. Watanabe, K. Ueno, A. Singh, G. Moody, F. Jahnke, X. Li, Twist angle-dependent interlayer exciton lifetimes in van der Waals heterostructures. *Phys. Rev. Lett.* **126**, 047401 (2021).
20. A. Arora, N. K. Wessling, T. Deilmann, T. Reichenauer, P. Steeger, P. Kossacki, M. Potemski, S. Michaelis de Vasconcellos, M. Rohlfing, R. Bratschitsch, Dark trions govern the temperature-dependent optical absorption and emission of doped atomically thin semiconductors. *Phys. Rev. B* **101**, 241413 (2020).
21. M. He, P. Rivera, D. Van Tuan, N. P. Wilson, M. Yang, T. Taniguchi, K. Watanabe, J. Yan, D. G. Mandrus, H. Yu, H. Dery, W. Yao, X. Xu, Valley phonons and exciton complexes in a monolayer semiconductor. *Nat. Commun.* **11**, 618 (2020).
22. J. Dang, S. Sun, X. Xie, Y. Yu, K. Peng, C. Qian, S. Wu, F. Song, J. Yang, S. Xiao, L. Yang, Y. Wang, M. A. Rafiq, C. Wang, X. Xu, Identifying defect-related quantum emitters in monolayer WSe_2. *npj 2D Mater. Appl.* **4**, 2 (2020).
23. J. R. Schaibley, P. Rivera, H. Yu, K. L. Seyler, J. Yan, D. G. Mandrus, T. Taniguchi, K. Watanabe, W. Yao, X. Xu, Directional interlayer spin-valley transfer in two-dimensional heterostructures. *Nat. Commun.* **7**, 13747 (2016).
24. A. F. Rigosi, H. M. Hill, Y. Li, A. Chernikov, T. F. Heinz, Probing interlayer interactions in transition metal dichalcogenide heterostructures by optical spectroscopy: MoS_2/WS_2 and $MoSe_2/WSe_2$. *Nano Lett.* **15**, 5033–5038 (2015).
25. T. Ye, J. Li, D. Li, Charge-accumulation effect in transition metal dichalcogenide heterobilayers. *Small* **15**, e1902424 (2019).
26. K. Tran, G. Moody, F. Wu, X. Lu, J. Choi, K. Kim, A. Rai, D. A. Sanchez, J. Quan, A. Singh, J. Embley, A. Zepeda, M. Campbell, T. Autry, T. Taniguchi, K. Watanabe, N. Lu, S. K. Banerjee, K. L. Silverman, S. Kim, E. Tutuc, L. Yang, A. H. MacDonald, X. Li, Evidence for moiré excitons in van der Waals heterostructures. *Nature* **567**, 71–75 (2019).
27. H. Park, J. Zhu, X. Wang, Y. Wang, W. Holtzmann, T. Taniguchi, K. Watanabe, J. Yan, L. Fu, T. Cao, D. Xiao, D. R. Gamelin, H. Yu, W. Yao, X. Xu, Dipole ladders with large Hubbard interaction in a moiré exciton lattice. *Nat. Phys.* **19**, 1286–1292 (2023).
28. Z. Lian, Y. Meng, L. Ma, I. Maity, L. Yan, Q. Wu, X. Huang, D. Chen, X. Chen, X. Chen, M. Blei, T. Taniguchi, K. Watanabe, S. Tongay, J. Lischner, Y.-T. Cui, S.-F. Shi, Valley-polarized excitonic Mott insulator in WS_2/WSe_2 moiré superlattice. *Nat. Phys.* **20**, 34–39 (2024).
29. H. Heo, J. H. Sung, S. Cha, B.-G. Jang, J.-Y. Kim, G. Jin, D. Lee, J.-H. Ahn, M.-J. Lee, J. H. Shim, H. Choi, M.-H. Jo, Interlayer orientation-dependent light absorption and emission in monolayer semiconductor stacks. *Nat. Commun.* **6**, 7372 (2015).
30. E. M. Alexeev, A. Catanzaro, O. V. Skrypka, P. K. Nayak, S. Ahn, S. Pak, J. Lee, J. I. Sohn, K. S. Novoselov, H. S. Shin, A. I. Tartakovskii, Imaging of interlayer coupling in van der Waals heterostructures using a bright-field optical microscope. *Nano Lett.* **17**, 5342–5349 (2017).
31. P. Rivera, J. R. Schaibley, A. M. Jones, J. S. Ross, S. Wu, G. Aivazian, P. Klement, K. Seyler, G. Clark, N. J. Ghimire, J. Yan, D. G. Mandrus, W. Yao, X. Xu, Observation of long-lived interlayer excitons in monolayer $MoSe_2/WSe_2$ heterostructures. *Nat. Commun.* **6**, 6242 (2015).
32. M. Baranowski, A. Surrente, L. Klopotowski, J. M. Urban, N. Zhang, D. K. Maude, K. Wiwatowski, S. Mackowski, Y. C. Kung, D. Dumcenco, A. Kis, P. Plochocka, Probing the interlayer exciton physics in a $MoS_2/MoSe_2/MoS_2$ van der Waals heterostructure. *Nano Lett.* **17**, 6360–6365 (2017).
33. M. H. Naik, E. C. Regan, Z. Zhang, Y.-H. Chan, Z. Li, D. Wang, Y. Yoon, C. S. Ong, W. Zhao, S. Zhao, M. I. B. Utama, B. Gao, X. Wei, M. Sayyad, K. Yumigeta, K. Watanabe, T. Taniguchi, S. Tongay, F. H. da Jornada, F. Wang, S. G. Louie, Intralayer charge-transfer moiré excitons in van der Waals superlattices. *Nature* **609**, 52–57 (2022).
34. X. Xu, W. Yao, D. Xiao, T. F. Heinz, Spin and pseudospins in layered transition metal dichalcogenides. *Nat. Phys.* **10**, 343–350 (2014).
35. W. T. Hsu, L. S. Lu, P. H. Wu, M. H. Lee, P. J. Chen, P. Y. Wu, Y. C. Chou, H. T. Jeng, L. J. Li, M. W. Chu, W. H. Chang, Negative circular polarization emissions from $WSe_2/MoSe_2$ commensurate heterobilayers. *Nat. Commun.* **9**, 1356 (2018).
36. X. Hong, J. Kim, S.-F. Shi, Y. Zhang, C. Jin, Y. Sun, S. Tongay, J. Wu, Y. Zhang, F. Wang, Ultrafast charge transfer in atomically thin MoS2/WS2 heterostructures. *Nat. Nanotechnol.* **9**, 682–686 (2014).
37. T. Yan, X. Qiao, P. Tan, X. Zhang, Valley depolarization in monolayer WSe_2. *Sci. Rep.* **5**, 15625 (2015).
38. M. Z. Maialle, E. A. de Andrada e Silva, L. J. Sham, Exciton spin dynamics in quantum wells. *Phys. Rev. B* **47**, 15776–15788 (1993).
39. J. Kim, C. Jin, B. Chen, H. Cai, T. Zhao, P. Lee, S. Kahn, K. Watanabe, T. Taniguchi, S. Tongay, M. F. Crommie, F. Wang, Observation of ultralong valley lifetime in WSe_2/MoS_2 heterostructures. *Sci. Adv.* **3**, e1700518 (2017).
40. K. Hao, G. Moody, F. Wu, C. K. Dass, L. Xu, C.-H. Chen, L. Sun, M.-Y. Li, L.-J. Li, A. H. MacDonald, X. Li, Direct measurement of exciton valley coherence in monolayer WSe_2. *Nat. Phys.* **12**, 677–682 (2016).
41. H. Zeng, J. Dai, W. Yao, D. Xiao, X. Cui, Valley polarization in MoS2 monolayers by optical pumping. *Nat. Nanotechnol.* **7**, 490–493 (2012).
42. J. Huang, T. B. Hoang, M. H. Mikkelsen, Probing the origin of excitonic states in monolayer WSe2. *Sci. Rep.* **6**, 22414 (2016).
43. T. Ye, Y. Li, J. Li, H. Shen, J. Ren, C. Z. Ning, D. Li, Nonvolatile electrical switching of optical and valleytronic properties of interlayer excitons. *Light Sci. Appl.* **11**, 23 (2022).
44. L. V. Butov, A. C. Gossard, D. S. Chemla, Macroscopically ordered state in an exciton system. *Nature* **418**, 751–754 (2002).
45. E. Liu, J. van Baren, C.-T. Liang, T. Taniguchi, K. Watanabe, N. M. Gabor, Y.-C. Chang, C. H. Lui, Multipath optical recombination of intervalley dark excitons and trions in monolayer WSe_2. *Phys. Rev. Lett.* **124**, 196802 (2020).
46. X. Wang, J. Zhu, K. L. Seyler, P. Rivera, H. Zheng, Y. Wang, M. He, T. Taniguchi, K. Watanabe, J. Yan, D. G. Mandrus, D. R. Gamelin, W. Yao, X. Xu, Moiré trions in $MoSe_2/WSe_2$ heterobilayers. *Nat. Nanotechnol.* **16**, 1208–1213 (2021).
47. T. Wang, S. Miao, Z. Li, Y. Meng, Z. Lu, Z. Lian, M. Blei, T. Taniguchi, K. Watanabe, S. Tongay, D. Smirnov, S.-F. Shi, Giant valley-zeeman splitting from spin-singlet and spin-triplet interlayer excitons in $WSe_2/MoSe_2$ heterostructure. *Nano Lett.* **20**, 694–700 (2020).
48. C. Jin, E. C. Regan, D. Wang, M. I. B. Utama, C.-S. Yang, J. Cain, Y. Qin, Y. Shen, Z. Zheng, K. Watanabe, T. Taniguchi, S. Tongay, A. Zettl, F. Wang, Identification of spin, valley and moiré quasi-angular momentum of interlayer excitons. *Nat. Phys.* **15**, 1140–1144 (2019).

49. P. K. Nayak, Y. Horbatenko, S. Ahn, G. Kim, J. U. Lee, K. Y. Ma, A. R. Jang, H. Lim, D. Kim, S. Ryu, H. Cheong, N. Park, H. S. Shin, Probing evolution of twist-angle-dependent interlayer excitons in $MoSe_2/WSe_2$ van der Waals heterostructures. *ACS Nano* **11**, 4041–4050 (2017).

Acknowledgments

Funding: This work was supported by the National Key Research and Development Program of China (grant no. 2021YFA1400700) and the National Natural Science Foundation of China (grants nos. 62025507, 11934019, 92250301, 62175254, 12174437, and 12204020). **Author contributions:** X.X., C.W., K.J., and Q.G. conceived and planned the project. D.D. and B.F. fabricated the devices. D.D., B.F., S.Y., X.C., H.L., and Z.Z. performed the optical measurements. D.D., J.Y., L.Y., B.F., and X.X. discussed the results and wrote the manuscript with contributions from other authors. **Competing interests:** The other authors declare that they have no competing interests. **Data and materials availability:** All data needed to evaluate the conclusions in the paper are present in the paper and/or the Supplementary Materials.

Submitted 17 January 2024
Accepted 12 April 2024
Published 15 May 2024
10.1126/sciadv.ado1281